Research papers

Modeling and prediction of lithium-ion battery thermal runaway via multiphysics-informed neural network

Sung Wook Kim [a], Eunji Kwak [b], Jun-Hyeong Kim [b], Ki-Yong Oh [b,*], Seungchul Lee [a,c,d,**]

[a] *Department of Mechanical Engineering, Pohang University of Science and Technology, 77 Cheongam-ro, Pohang, Republic of Korea*
[b] *Department of Mechanical Convergence Engineering, Hanyang University, 222 Wangsimni-ro, Seongdong-gu, Seoul, Republic of Korea*
[c] *Graduate School of Artificial Intelligence, Pohang University of Science and Technology, 77 Cheongam-ro, Pohang, Republic of Korea*
[d] *Institute of Convergence Research and Education in Advanced Technology, Yonsei University, 50 Yonsei-ro, Seoul, Republic of Korea*

ARTICLE INFO

ABSTRACT

In this study, a multiphysics-informed neural network (MPINN) is proposed for the estimation and prediction of thermal runaway (TR) in lithium-ion batteries (LIBs). MPINNs are encoded with the governing laws of physics, including the energy balance equation and Arrhenius law, ensuring accurate estimation of time and space-dependent temperature and dimensionless concentration in comparison to a purely data-driven approach. Specifically, the network is trained using data from a high-fidelity model of an LIB, which describes TR by addressing several coupled partial differential equations. Quantitative analysis reveals that the mean absolute error (MAE) and root mean squared error (RMSE) of the MPINN for TR estimation are less than an artificial neural network (ANN) by 0.71 and 1.57, respectively, when using fully labeled data for training. It outperforms the ANN in terms of MAE and RMSE by 90.56 and 118.64, when only a small portion of labeled data (semi-supervision) are used for TR prediction. Importantly, it predicts TR without any labeled data when the decomposition of reactive species is modeled in the positive electrode. The MPINN exhibits promising results in surrogate modeling, implying it can be successfully implemented in practical scenarios and stimulate further research related to TR modeling using physics-informed deep learning.

1. Introduction

The advent of various electric vehicles (EVs) has led to the widespread adoption of lithium-ion batteries (LIBs) as a primary source of energy. The current form of LIBs is favorable over other types owing to its EV-friendly characteristics, including high energy density, long duration, and fast charge rate. Nevertheless, LIBs encounter limitations in expanding their territory owing to safety and reliability concerns. The primary safety concern in LIBs is thermal runaway (TR), which refers to an irreversible state in LIBs wherein owing to an internal short circuit (ISC) at the initial stage, the local cell temperature rises and leads to combustion until the internal reactive species of LIB components are burned. TR is hazardous in industrial applications because it may lead to explosion in LIBs; in other words, irreversible and exothermic reactions in LIBs may result in fire, explosion, and even mass mortality [1].

On-time prognosis of TR and estimation of the TR phenomenon under various operational conditions is an active field of research because it not only enables TR forecast, but also provides information regarding the optimal design of LIB structures (for example, the surface-to-volume ratio) such that TR is restrained or mitigated when LIBs are exposed to charge, discharge, and external conditions of the daily routine or extremely harsh conditions. Because TR is characterized by several factors and chain reactions, including thermodynamics, chemical reaction degradation of each component, and aging, multiphysics along with these phenomena should be considered when modeling TR. Ping et al. [2] presented an electrothermal model in which electric conduction was coupled with heat transfer and energy balance. The evolution process of TR was investigated using the OpenFOAM software under various conditions, including different discharge rates, airflow velocities, ambient temperatures, and airflow channel thicknesses.

Kwak et al. [3] coupled three multiphysics phenomena, including aging, thermodynamics, and chemical degradation, to investigate TR pathways under several abuse conditions. The aging model was shown to influence the peak and onset temperatures under electrical and thermal abuse conditions. TR has also been investigated under particular abuses, including nail penetration [4,5], overcharge [6], external short circuit [7,8], ultra-high discharge rates [8], and pack-level propagation [9]. It should be noted that the computation time is essential for preventing TR or reducing the experimental cost during control enabling solutions and design optimization in LIB cells, modules, and packs; however, all previous studies relied on numerical simulations, such as the finite element method (FEM) and finite difference method (FDM), that require significant computational effort. In other words, conventional modeling tools cannot be used readily to predict or estimate TR in a stochastic and rapidly changing environment and under various practical operational conditions encountered by LIBs. In addition, they cannot be used more effectively during system and design optimization owing to their considerable computational time (hours to several days, depending on the complexity of the multiphysics model of LIBs).

Physics-informed neural networks (PINNs) have been extensively studied in recent years as a prospective surrogate model for numerous time-dependent systems in engineering with the goal of replacing the traditional FEM/FDM. The major advantage of PINNs is that they are capable of rapidly modeling time-dependent systems of interest without losing generality and accuracy. Fundamentally, PINNs are different from ordinary data-driven deep learning models because they are trained in conjunction with the governing laws of physics to ensure that they do not violate these laws and produce results that are robust to outliers. This also implies that the governing laws of physics effectively supervise neural networks along with the given data, thus increasing the probability of approaching the global minimum from an optimization perspective. Hence, the estimation results are interpretable and physically reasonable. In contrast to the FEM/FDM, which requires a separate long training session for each operating condition or control variable, PINNs are trained to meet the requirements represented by the governing equations of a time-dependent system in the beginning, which allows them to output system response at any given operating condition. For example, Sun et al. [10] leveraged a PINN to solve parameterized geometries in a fluid flow problem, wherein multiple geometry designs were solved simultaneously at a reduced computational cost. Owing to their mesh-free nature, PINNs can ultimately be agnostic to the geometry, boundary, and initial conditions, albeit with several restrictions. Such characteristics can significantly reduce the amount of time and effort required to evaluate product performance and durability under diverse conditions.

Prior studies regarding PINN-based estimation are manifold and their applications cover a wide range of engineering fields, including fluid mechanics, heat transfer, geophysics, biomedicine, structural mechanics, and reaction kinetics. Raissi et al. [11] proposed a physics-informed deep learning framework to infer physical quantities, such as velocity and pressure fields, in complex domains, such as human arteries and brain aneurysms, in both 2D and 3D settings. The partial differential equations (PDEs) involved in their study were the well-known Navier-Stokes equations, whose numerical computation time is long. The training data were retrieved from numerical results, for which direct measurements may not be possible, and the regression results of the suggested algorithm were highly similar to the reference data. Niaki et al. [12] presented a PINN to estimate the thermochemical evolution of a composite material. The proposed model consisted of two distinct networks for learning different physics, which were trained sequentially because the two physical laws are coupled in time. In addition, they were trained using a technique called adaptive learning rate annealing to overcome the possible stiffness present between the loss terms of the objective function. Similarly, Cai et al. [13] addressed the general heat transfer problems of industrial complexity by considering forced and mixed convection scenarios. To solve the renowned two-phase Stefan

problems that involve the joint evolution of a liquid and solid and their moving phase transition interface, the first network inferred the spatiotemporal temperature fields of both the liquid and solid, while the second network predicted the moving interface over time. Some of the derivative terms of the network outputs were connected by the heat equation and Stefan conditions. The aforementioned case studies investigated the feasibility and effectiveness of replacing the traditional FEM/FDM with PINNs in the near future, and several presented promising results under particular assumptions or restrictive conditions.

Nevertheless, to the best of our knowledge, no study has reported the application of PINNs for estimating the TR in LIBs thus far. More importantly, only a few PINN-related studies have discussed the depth of surrogate modeling and possibly substituted the FEM/FDM. This is mainly because PINNs do not necessarily guarantee the perfect conformation of unseen data points to the governing equations, despite learning the equations during network optimization. Moreover, it has been discovered that the convergence of PINNs during training depends significantly on the type of physics involved [14–17]. In other words, PINNs are vulnerable to out-of-distribution data, similar to most deep-learning models, because the governing equations are provided as soft constraints in the objective function. Moreover, investigations related to solving complex multiphysics dynamics with singularities are limited because they are more challenging and stiffer to solve from a mathematical standpoint using PINNs owing to the highly non-convex nature of the loss function and the imbalance caused when optimizing multiple loss functions simultaneously. Inspired by PINN applications in other disciplines, a PINN is first developed exclusively for the estimation and prediction of TR, which involves a complex thermochemical multiphysics phenomenon with a sharp inflection point at the TR. Subsequently, its feasibility as a surrogate model for the FEM/FDM under diverse operating conditions for its broad implementation ranging from design optimization to on-board vehicle battery management is investigated. The contributions of this study are summarized below:

1. To the best of our knowledge, this is the first study that comprehensively investigated the use of a multiphysics-informed neural network (MPINN) to estimate and predict TR in LIBs. Estimating the multiphysics nature of TR was resolved by assigning an independent network for modeling each dynamics simultaneously undergoing a different optimization process. However, different dynamics should be coupled at each iteration step during optimization. Therefore, an MPINN was used instead of a single PINN for TR estimation.
2. This study discussed the effects of a commonly adopted technique for PINN optimization, i.e., learning rate annealing, and data-fit loss for the faster convergence of MPINN to estimate TR. The estimation results indicated that the use of learning rate annealing and data-fit loss reduced the overall error.
3. This study also highlighted the challenges and solutions involved in estimating TR induced by the degradation of different types of chemically reactive species. Based on the results presented in Section 4, the MPINN exhibited better performance for less-sophisticated chemical reactions.
4. The MPINN was compared with the output of a numerical simulation software (hereafter referred to as the reference data) and deep neural network (DNN) with equivalent structure in various aspects to emphasize the advantages of the MPINN as a potential alternative to the conventional FEM/FDM.

The remainder of this paper is organized as follows. Section 2 introduces the TR mechanism, proposed MPINN model, and implementation details. Section 3 discusses the details of the data generation process using a numerical simulation software and the experimental design. Section 4 presents the overall results to compare the performance of MPINN against a standard DNN as a potential surrogate model of the numerical simulation method. Finally, Section 5 concludes the

study with a quantitative and qualitative summary.

2. Multiphysics-informed neural network

2.1. Multiphysics of thermal runaway

TR in an LIB refers to the occurrence of successive chain reactions of component degradation owing to temperature rise from exothermic reactions or increased current flow and power dissipation [8]. It is a complex multiphysics phenomenon in which many physical phenomena contribute to the exothermic reaction. The thermodynamics and chemical reaction in TR can be formulated as follows:

$$\rho C_p \frac{\partial T(x,t)}{\partial t} = \nabla k \nabla T + \dot{Q}_{exo}, x \in \Omega, t \in [0, t_{max}] \tag{1}$$

where ρ, C_p, T, k, and Ω denote the cell density, heat capacity, temperature, thermal conductivity coefficient, and subset of R^D, respectively. Eq. (1) represents the energy balance equation that describes the rate of temperature change on the left-hand side and heat conduction, along with the volumetric heat generation rate, $\dot{Q}_{exo}$, originating from an exothermic reaction due to stimulated chemical reaction on the right-hand side. Note that the third term of the equation, $\dot{Q}_{exo}$, defined by Eq. (2), is a new contribution to the energy balance equation, which is proportional to the rate of dimensionless concentration change.

$$\dot{Q}_{exo} = HWR = HW\left(-\frac{\partial c(x,t)}{\partial t}\right) = HWAexp\left(-\frac{E}{R_c T}\right)c^m, x \in \Omega, t \in [0, t_{max}] \tag{2}$$

where H, W, R, c, A, E, R_c, and m denote the specific heat release, specific active material content per volume, reaction rate, dimensionless concentration of lithium in electrolyte, frequency factor of electrolyte decomposition, thermal activation energy, gas constant, and reaction order, respectively. Eq. (3) describes the convectional heat exchange between an LIB and external environment:

$$k \nabla T = h(T_{amb} - T), x \in \partial\Omega \tag{3}$$

where h and T_{amb} denote the convective heat transfer coefficient and ambient temperature, respectively. Finally, Eq. (4) presents the initial condition of the temperature and dimensionless concentration of lithium ions in electrolyte defined over the entire computational domain Ω as follows:

$$T(x, t=0) = T_0, c(x, t=0) = c_0, x \in \Omega \tag{4}$$

TR modeling requires solving the aforementioned governing equations by providing the distributions of temperature T and dimensionless concentration c as a function of space x, time t, and ambient temperature T_{amb}.

Exothermic reactions triggered by a sequential chemical degradation of the four components of lithium-ion batteries is known to account for the rapid temperature escalation during thermal runaway. The chemical degradation occurs in the following order: solid electrolyte interphase (SEI), negative electrode, positive electrode, and electrolyte. The heat generated via the exothermic reactions is simply the addition of each contribution and it is represented as the following equation:

$$\dot{Q}_{exo} = \dot{Q}_{SEI} + \dot{Q}_{ne} + \dot{Q}_{pe} + \dot{Q}_e \tag{5}$$

In this study, only the positive electrode decomposition model ($\dot{Q}_{pe}$) and the electrolyte decomposition model ($\dot{Q}_e$) are investigated separately because adding up all four models requires excessive computation, and the two models are known to be the major contributors to the heat generation leading up to TR. More importantly, a precise estimation of TR that reflects the reality is beyond the scope of this study, and it is to be done in future work. For the two models, R_{pe} and R_e are represented

by the following Arrhenius law:

$$R_{pe} = \frac{d\alpha}{dt} = A_{pe}\alpha^{m_{pe}^p}(1-\alpha)^{m_{pe}^r}exp\left(-\frac{E_{a,pe}}{RT}\right) \tag{6}$$

$$R_e = -\frac{dc_e}{dt} = A_e exp\left(-\frac{E_{a,e}}{RT}\right)c_e^{m_e}. \tag{7}$$

As the equations describing the reaction rates of the models are different, this leads to significant difference in the rates as time passes and temperature reaches a certain level, explaining the fundamental difference in resultant temperature between the positive electrode decomposition model and the electrolyte decomposition model as shown throughout Section 4.

2.2. Formulation of MPINN

A general PINN approximates a solution of a PDE by adding the equation as a penalty term or constraint to the empirical loss function of a DNN such that data fitting and the governing equation are satisfied after parameter optimization; the model output is equal to the solution of the equation or system response of a time-dependent system. Similarly, to establish a PINN framework for modeling TR, Eqs. (1)–(4) should be added as penalty terms to the empirical loss function. From this perspective, Eqs. (3) and (4) are the boundary and initial conditions, respectively, which lead to a unique solution for the governing PDE of Eq. (1). Such physics-based constraints are often referred to as residual loss, whereas empirical loss is often referred to as data-fit loss. Ideally, optimization is complete when each residual and data-fit loss equals zero, implying that the governing laws of physics, boundary conditions, and initial conditions are satisfied. Meanwhile, a thermochemical reaction is involved in the case of TR, indicating that the heat transfer and heat generation dynamics caused by chemical reactions interact, with a differential equation describing each dynamic. It is worth noting that these physics-related factors co-supervise the neural network with the given data, thereby improving the accuracy and robustness of the PINN. Therefore, TR estimation through a PINN requires a distinct network for modeling each dynamic separately and simultaneously; hence, the name, MPINN, of the specific model. Following the predominant approach of a PINN, the total loss, L, of the MPINN can be expressed as:

$$L = \lambda_1 L_D + \lambda_2 L_{PDE} + \lambda_3 L_{ODE} + \lambda_4 L_{BC} + \lambda_5 L_{IC} \tag{8}$$

where L_D, L_{PDE}, L_{ODE}, L_{BC}, and L_{IC} denote the data-fit loss, PDE loss, ordinary differential equation (ODE) loss, boundary-condition loss, and initial-condition loss, respectively, which are defined as:

$$L_D = \left\|\widehat{T} - T\right\|_{\Omega \times [0,L]}^2 + \left\|\widehat{c} - c\right\|_{\Omega \times [0, t_{max}]}^2 \tag{9}$$

$$L_{PDE} = \left\|\rho C_p \frac{\partial \widehat{T}(x,t)}{\partial t} - \nabla k \nabla \widehat{T} - \dot{Q}_{exo}\right\|_{\Omega \times [0, t_{max}]}^2 \tag{10}$$

$$L_{ODE} = \left\|\frac{\partial \widehat{c}(x,t)}{\partial t} + Aexp\left(-\frac{E}{R_c \widehat{T}}\right)\widehat{c}^m\right\|_{\Omega \times [0, t_{max}]}^2 \tag{11}$$

$$L_{BC} = \left\|k\nabla\widehat{T} - h(T_{amb} - \widehat{T})\right\|_{\partial\Omega \times [0, t_{max}]}^2 \tag{12}$$

$$L_{IC} = \left\|\widehat{T}_0 - T_0\right\|_{\Omega \times \{t=0\}}^2 + \left\|\widehat{c}_0 - c_0\right\|_{\Omega \times \{t=0\}}^2. \tag{13}$$

It should be noted that the definitions of constants and variables in these equations have been addressed previously. In particular, λ_* is the relative weighting coefficient of each loss function. In addition, $\|\bullet\|^2$ refers to the mean squared error (MSE) of a set of collocation points defined over a specified range. For example, $\|k\nabla\widehat{T} - h(\widehat{T} - T_{amb})\|_{\partial\Omega \times [0, t_{max}]}^2$ denotes the MSE evaluated along the Neumann boundary, i.e., $\partial\Omega \times [0,$

t_{max}]. In the above formulation, the loss terms, except L_D, may be considered as penalty terms. Eq. (12) states a Neumann boundary condition that is a function of T_{amb}, i.e., a control variable that determines the rate of temperature change. It is important to note that the data-fit loss (Eq. (9)) can sometimes be omitted in previously reported cases [10,13,16]. This study investigates the effect of its presence, which is further discussed in Section 4.

Considering the loss formulation of the MPINN, the network structure of the proposed MPINN is illustrated in Fig. 1; x, y, t, and T_{amb} are the inputs of the network. Because two physical quantities must be estimated for TR modeling, two distinct networks were used, namely, *Network T* and *Network C*, that shared the same input; the former and latter learn and output the temperature (T) and dimensionless concentration of reactive species (c), respectively, given the inputs. The network outputs are then used to calculate the partial derivative terms by automatic differentiation [18] followed by the computation of loss terms. Importantly, the PDE loss, i.e., the energy-balance equation, couples the outputs of the two distinctively trained networks, enabling it to consider the multiphysics characteristics of TR. Hence, the main difference between the proposed MPINN and a single PINN lies in the structure with interconnected loss functions. Note that $\alpha_1 = k_x t_{max}/x_{max}^2 \rho C_p$, $\alpha_2 = k_y t_{max}/y_{max}^2 \rho C_p$, $\alpha_3 = HW/T_{max}\rho C_p$, $\beta = t_{max}A$, $\gamma_1 = k_x/hx_{max}$, and $\gamma_2 = k_y/hy_{max}$. The loss terms are multiplied by the adaptive weighting coefficients, λ_*, and added to calculate the total loss, L. `Based on the total loss, L, the error is backpropagated to further optimize the network parameters. The hyper-parameters involved in the training are given as follows. A single network consists of an input layer of 4 nodes, 6 hidden layers of 20 nodes, and an output layer of a single node. The specified numbers regarding the network structure are determined heuristically through numerous experimentations. The number of training data used for optimizing the network parameters are 1,271,571 for the data-fit loss, 1,132,400 for the PDE loss, 68,571 for the boundary condition loss, and 3171 for the initial condition loss. The size of training set for the loss terms vary because each loss term can be minimized using only the samples fetched from the domain of interest. For example, the boundary condition loss is minimized using data points along the boundaries of the domain, which critically reduces the number of trainable samples compared with the case of the data-fit loss. The batch size and the learning rate are set to 15,000 and 1e-3, respectively. The network was programmed using Python 3.5.2, TensorFlow 1.14.0, and Keras 2.2.5. The computations were performed using a GeForce RTX 2080TI GPU.

2.3. Training algorithm

Training a PINN is a challenging task that remains an active research topic. This is because PINNs encounter convergence issues owing to failure modes originating from the type, nonlinearity, and number of physics involved. It has been reported that PINNs fail to converge near the global minimum owing to the complex loss landscape [14], unbalanced backpropagated gradients [15], and slow convergence [16]. Some widely known nonlinear and high-order PDEs that fail to accurately converge include the Allen–Cahn and Cahn–Hilliard equations. Therefore, numerous techniques, such as curriculum regularization [14], sequence-to-sequence learning [14,19], sequential training [12], variational or weak-form PDE regularization [20–22], domain decomposition [21,23], adaptive activation function [23], learning rate annealing [12,24], and PINN-specialized optimizers [25] have been proposed or exploited to overcome the failure modes. However, such workarounds are applicable to specific PDEs [14,15,17] and, to the best of our knowledge, no solution has yet been introduced to solve a family of general PDEs with varying boundary and initial conditions, which is currently the main limitation of PINN-based modeling in comparison to FEM/FDM. Investigating the existing approaches is beyond the scope of this study. However, most PINNs encounter a common convergence issue originating from the presence of multiple loss functions with different minimization speeds. Learning rate annealing [15], which was devised to address this issue, is relatively intuitive and easy to follow. Thus, it has been presented to address the TR problem in this study.

Learning rate annealing adaptively rebalances the weighting coefficients, λ_i, specified in the total loss function of Eq. (8). When minimizing the loss function, some loss terms tend to be minimized faster than others owing to differences in convexity [15,24] and scale [16]. This phenomenon typically results in slower convergence and poor local minima. The former issue is generally resolved by tuning the parameter $\lambda_i^{(n)}$, where subscript n denotes the iteration number at each training iteration, to balance the contribution of each term to the total loss. Algorithm 1 describes the modification of the weighting coefficients at each training iteration in a pseudo-code format.
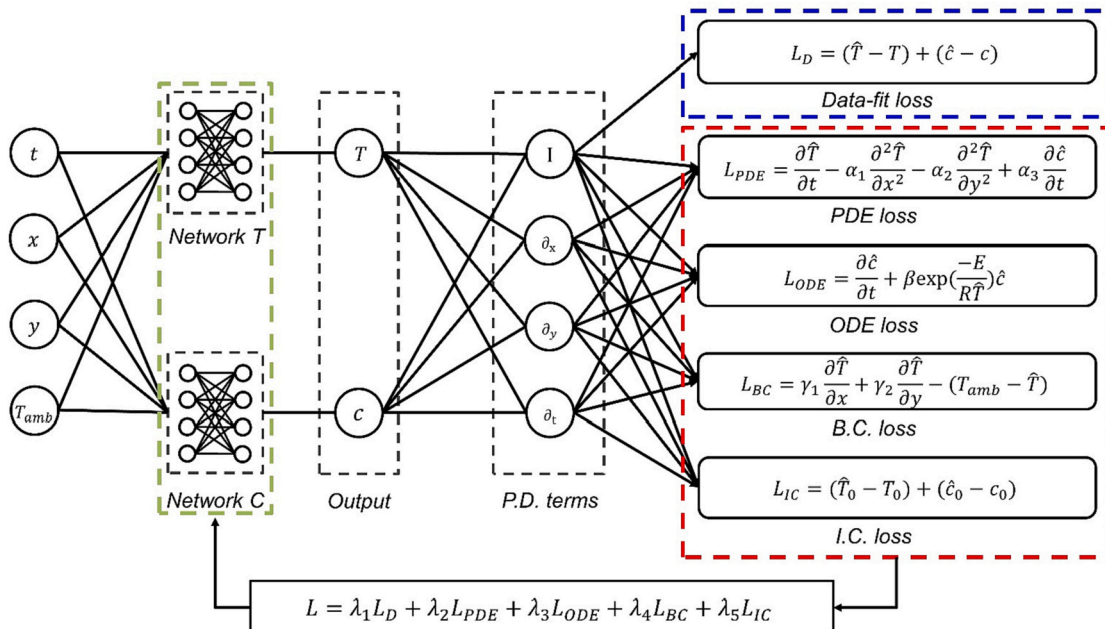

Fig. 1. Graphical illustration of the MPINN structure and model optimization.

Algorithm 1. Learning rate annealing

Assume a PINN with the following loss function, where i and n denote the loss function index (excluding PDE loss) and training iteration index, respectively.

$$L(\theta) = L_{PDE}(\theta) + \lambda_i^{(n)} L_i(\theta). \qquad (14)$$

For $i = 1, \ldots, M$ and $n = 1, \ldots, S,$

(1) Compute

$$\bar{\lambda}_i^{(n)} = \frac{max\left(\left|\nabla_\theta L_{PDE}\left(\theta^{(n)}\right)\right|\right)}{mean\left(\left|\nabla_\theta L_i\left(\theta^{(n)}\right)\right|\right)}. \qquad (15)$$

(2) Update the weights

$$\lambda_i^{(n)} = \alpha \bar{\lambda}_i^{(n)} + (1 - \alpha)\bar{\lambda}_i^{(n-1)} \qquad (16)$$

End

α denotes the exponential moving average decay that is normally set to 0.9.

Specifically, Eq. (14) is another expression of Eq. (8), with $\lambda_2 = 1$. The gradient of PDE loss generally exhibits the largest value owing to the high nonlinearity of the function. Therefore, other loss terms must be assigned weight coefficients larger than one ($max(|\nabla_\theta L_{PDE}(\theta^{(n)})|) \geq mean(|\nabla_\theta L_i(\theta^{(n)})|)$). New weight coefficients are determined (Eq. (15)) and updated in each iterative training loop considering the new coefficients ($\bar{\lambda}_i^{(n)}$) and those from the previous loop ($\bar{\lambda}_i^{(n-1)}$). During weight update, the two terms are weighted by the exponential moving average decay to provide an averaging effect (Eq. (16)).

The difference in the scale of input and output is another factor contributing to weight imbalance between the loss terms. Unlike purely data-driven deep learning models, PINN setups encounter problems when the network output is scaled but physics residual loss terms, such as PDE loss, are unscaled. To eliminate the mismatch between the normalized network output of the physical quantity and PDEs with physical dimensions, the variables and coefficients of PDEs should also be normalized and nondimensionalized. To scale the loss in Eqs. (1)–(4), nondimensionalization [26,27], which removes physical dimensions by substituting variables, is used as follows:

$$
\begin{aligned}
x^* &= \frac{x - x_{min}}{x_{max} - x_{min}}, \\
y^* &= \frac{y - y_{min}}{y_{max} - y_{min}}, \\
T^* &= \frac{T}{T_{max}}, \\
c^* &= c, \\
t^* &= \frac{t}{t_{max}}
\end{aligned} \qquad (17)
$$

where x^*, y^*, T^*, c^*, and t^* denote the dimensionless quantities of their counterparts. Their values range from zero to one and are provided as inputs to the model in Fig. 1. The nondimensionalization results of Eqs. (18)–(20) are the new dimensionless equations.

$$\rho C_p \frac{T_{max}}{t_{max}} \frac{\partial T^*}{\partial t^*} = k_x \frac{T_{max}}{x_{max}^2} \frac{\partial^2 T^*}{\partial x^{*2}} + k_y \frac{T_{max}}{y_{max}^2} \frac{\partial^2 T^*}{\partial y^{*2}} - \frac{HW}{t_{max}} \frac{\partial c^*}{\partial t^*} \qquad (18)$$

$$k_x \frac{T_{max}}{x_{max}} \frac{\partial T^*}{\partial x^*} + k_y \frac{T_{max}}{y_{max}} \frac{\partial T^*}{\partial y^*} = h T_{max}\left(T_{amb}^* - T^*\right) \qquad (19)$$

$$T^*(x, t = 0) = \frac{T_0}{T_{max}}, c^*(x, t = 0) = c_0 \qquad (20)$$

3. Experiment

Fig. 2 illustrates the proposed framework for TR estimation and prediction using MPINN. First, a sufficient amount of data was generated through a high-fidelity model using COMSOL Multiphysics 5.6. The MPINN was then fed with the data for training. The model comprised two different networks to consider the multiphysics in TR. *Network T* was trained to learn the evolution of temperature distribution over space and time, whereas *Network C* was set to learn the concentration of reactive species that degrade over time due to temperature increase.
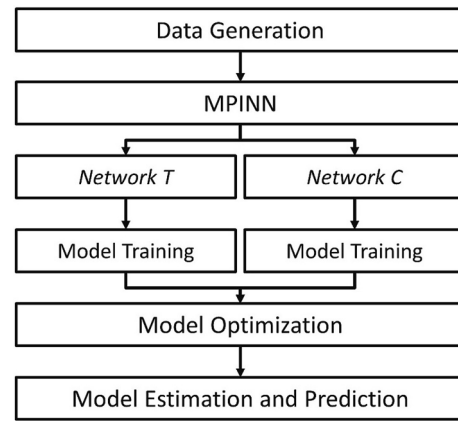

Fig. 2. Flowchart of MPINN-based TR estimation and prediction of LIB.

Each network was assigned a different task; thus, a different objective function was required by each network. However, the networks were optimized simultaneously because they were coupled with one another by the total governing equation. After successful optimization, the results were visualized and analyzed, as described in Section 4.

3.1. Experimental design

TR in an LIB is a multiphysics phenomenon, wherein numerous factors contribute to the elevation in temperature. Previous studies have reported various models involving aging characteristics [3], Joule heating [28], heat generation in the SEI layer [29–31], negative electrode [29–31], positive electrode [29,31], and electrolyte [29,31]. However, a precise estimation of TR that reflects the reality is beyond the scope of this study. For the sake of model simplicity, a cylindrical lithium-ion cell was assumed to be heated inside an insulated oven without any charge or discharge process, implying that there was no electrochemical heat source but only an exothermic heat source from thermal abuse. In practical applications, this is equivalent to a situation in which heat is propagated between several stacked batteries. Therefore, this study focused mainly on a scenario where exothermic heat is generated only by electrolyte decomposition, which is the main contributing factor to the instant rise in temperature during TR. However, a special case of a chemical reaction in the positive electrode has also been investigated in Section 4 for a comparative analysis of the MPINN. The two chemical reactions cannot be modeled simultaneously because they increase the computational complexity, which leads to failure in MPINN convergence, a limitation of MPINNs, as stated in Section 2.3. Thus, a more precise TR model will be explored in future research. Constants H, W, R, A, and E are properties that rely on the type of species of interest, and they are adjusted to the case of electrolyte in this study; moreover, ρ and C_p are isotropic thermal properties and k is

Table 1
Thermochemical properties for TR estimation.

Property	Abbreviation	Value
Thermal conductivity in angular direction [$W/(m \bullet K)$]	k_a	140
Thermal conductivity in radial direction [$W/(m \bullet K)$]	k_r	0.7
Initial temperature [$°C$]	T_0	25
Cell density [kg/m^3]	ρ	2231.2
Heat capacity [$J/(kg \bullet K)$]	C_p	1100
Heat transfer coefficient [$W/(m^2 \bullet K)$]	h	12
Gas constant [$J/(mol \bullet K)$]	R_c	8.314
Activation energy value of electrolyte [J/mol]	E	2.7e+5
Reaction factor of electrolyte [$1/s$]	A	5.14e+25
Reaction order of electrolyte	m	1
Initial dimensionless concentration	c_0	1
Heat released [J/kg]	H	6.2e+5
Specific active material content [kg/m^3]	W	335

an anisotropic property that varies depending on the direction. Table 1 summarizes the thermochemical properties obtained from [3], modeling a commercial Lithium iron phosphate (LFP) cell.

3.2. Data generation through numerical simulation

COMSOL Multiphysics 5.6 is a popular FEM-based software that features various modules to help users simulate heat transfer, electro-chemistry, aerodynamics, and fluid dynamics. Numerous studies [3,28,32,33] have reported applications related to LIB simulation using this software owing to its ease of use and high modeling capability. Inspired by prior examples, the same software was used in this study to generate reference data.

To numerically solve the TR problem, a simplified yet accurate geometric assumption was made (Fig. 3(a)), followed by mesh creation over the computational domain (Fig. 3(b)). A 3D cylindrical cell can be computed efficiently using a 2D axisymmetric model, wherein a single rectangular cross-section is computed. The outcome was rotated 360° with respect to the axis of rotation (located at $r = 0$) to retrieve the 3D model in polar coordinates. Quadratic meshes were used in finite element analysis, and a total of 1560 meshes were created. To account for the multiphysics in TR, two distinct sub-models, i.e., the heat transfer module and distributed ODE interface featured within the software, were built. In the TR model, the heat transfer theory and exothermic heat generation from the active materials of an LIB were coupled. They were merged such that the initial temperature, T_0, became the first input to the chemical reaction model to obtain $\dot{Q}'_{exo}$, which was then fed into the heat transfer model to obtain T'_{cell}.

4. Results and discussion

4.1. Multiphysics phenomena of TR

To understand the multiphysics phenomena of TR in an LIB, TR in a cylindrical LIB was estimated using COMSOL Multiphysics 5.6, as described in Section 3.2. The estimated results with the input ambient temperature (Fig. 4(a)) included the mean temperature (Fig. 4(b)), mean dimensionless concentration of lithium in the electrolyte (Fig. 4(c)), mean reaction rate (Fig. 4(d)), and temperature change rate (Fig. 4(e)). Specifically, the ambient temperature, T_{amb}, was constant at 308.15 K until t=60 min, when it linearly increased to 473.15 K until t=90 min (Fig. 4(a)). The remaining computation time was kept constant at 473.15 K. The increase in ambient temperature affected the LIB temperature and stimulated an internal chemical chain reaction. Even after

the ambient temperature became 473.15 K (=200 °C) at t=90 min, the temperature continued to rise until the TR reached the maximum temperature of 543.84 K at t=224 min, implying that the given ambient temperature was sufficient for the cell to reach the crucial temperature, thereby initiating exothermic chemical degradation of the electrolyte. This temperature elevation in the LIB resulted in the evolution of dimensionless concentration of reactive species, which started from t=168 min near the onset temperature (Fig. 4(c)), indicating the onset of electrolyte decomposition . The reaction rate shown in Fig. 4(d) implies an inverse behavior compared to the dimensionless concentration, and it mainly focuses on the rapidly generated heat before the TR. Lastly, Fig. 4 (e) plots the temperature change rate (C/min) against the temperature (K). It shows that the onset temperature, defined as the point where the self-heating becomes prominent, occurred at $t = 184$ min and $T = 468.9$ K, and the crucial temperature, defined as the point where the self-heat rate exceeds 2 °C/min, occurred at $t = 218.3$ min and $T = 489.1$ K. This point is often regarded as the beginning of the thermal runaway. It takes 34.3 min from the point of the onset temperature to reach the crucial temperature. The maximum temperature ($T = 543.48$ K) is reached at $t = 222.6$ min. It takes 38.6 min from the start of the point of the onset temperature to reach the maximum temperature, and it takes 4.6 min from the start of the point of the critical temperature to reach the maximum temperature.

Fig. 5 illustrates the results depicting the evolution of temperature distribution over space and time. It should be noted that the figure intends to show the varying spatial temperature gradient across the cy-lindrical cell at sequential time steps; therefore, the scale bar at each time step changes accordingly. At t=85 min, it can be observed that the cell temperature closer to the boundary, in other words, the surface temperature increases with the ambient temperature. This is the TR propagation stage from the external environment. Moreover, chemical reactions and electrolyte decomposition can be observed at the center of the cell starting at t=168 min, leading to a relatively higher temperature at the center. This is regarded as the point of exothermic onset, from which exothermic reactions become more dominant than heat escaping from a cell, leading to a heat-temperature-reaction loop [34]. Subsequently, the generated heat was propagated outward toward the boundaries at t=179 min. Finally, at t=233 min, the temperature was evenly distributed across the entire domain after going through the peak temperature, and all reactants in the electrolyte were consumed. The temperature at the outer surface of the cell was slightly lower owing to the persistent heat exchange with the external environment. It should be noted that the acquired data have been used as reference data for comparative purposes in the following subsections.
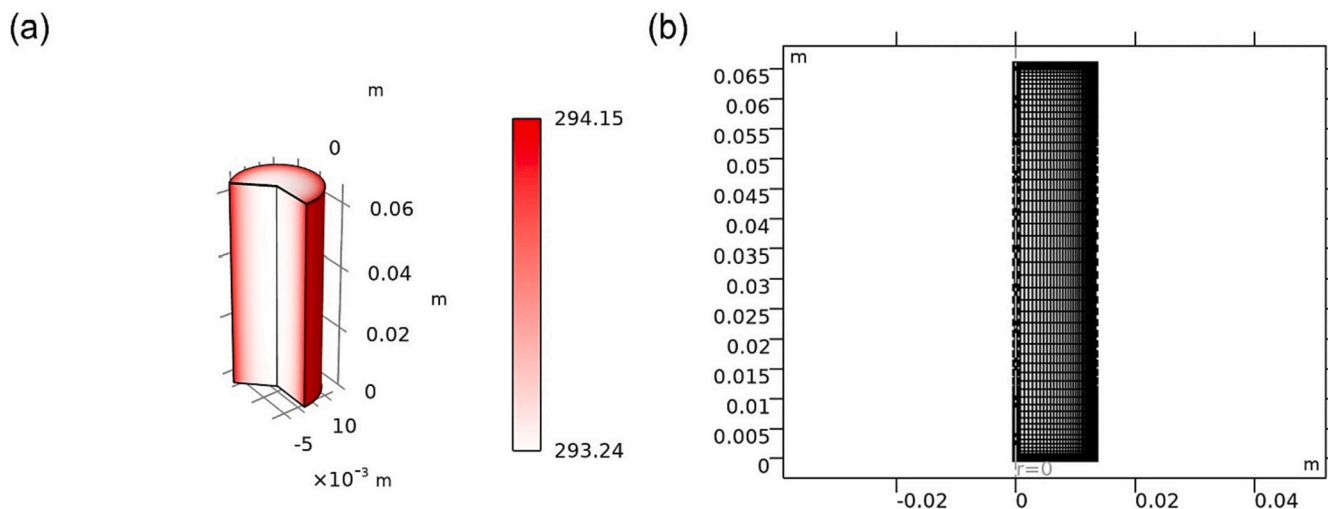

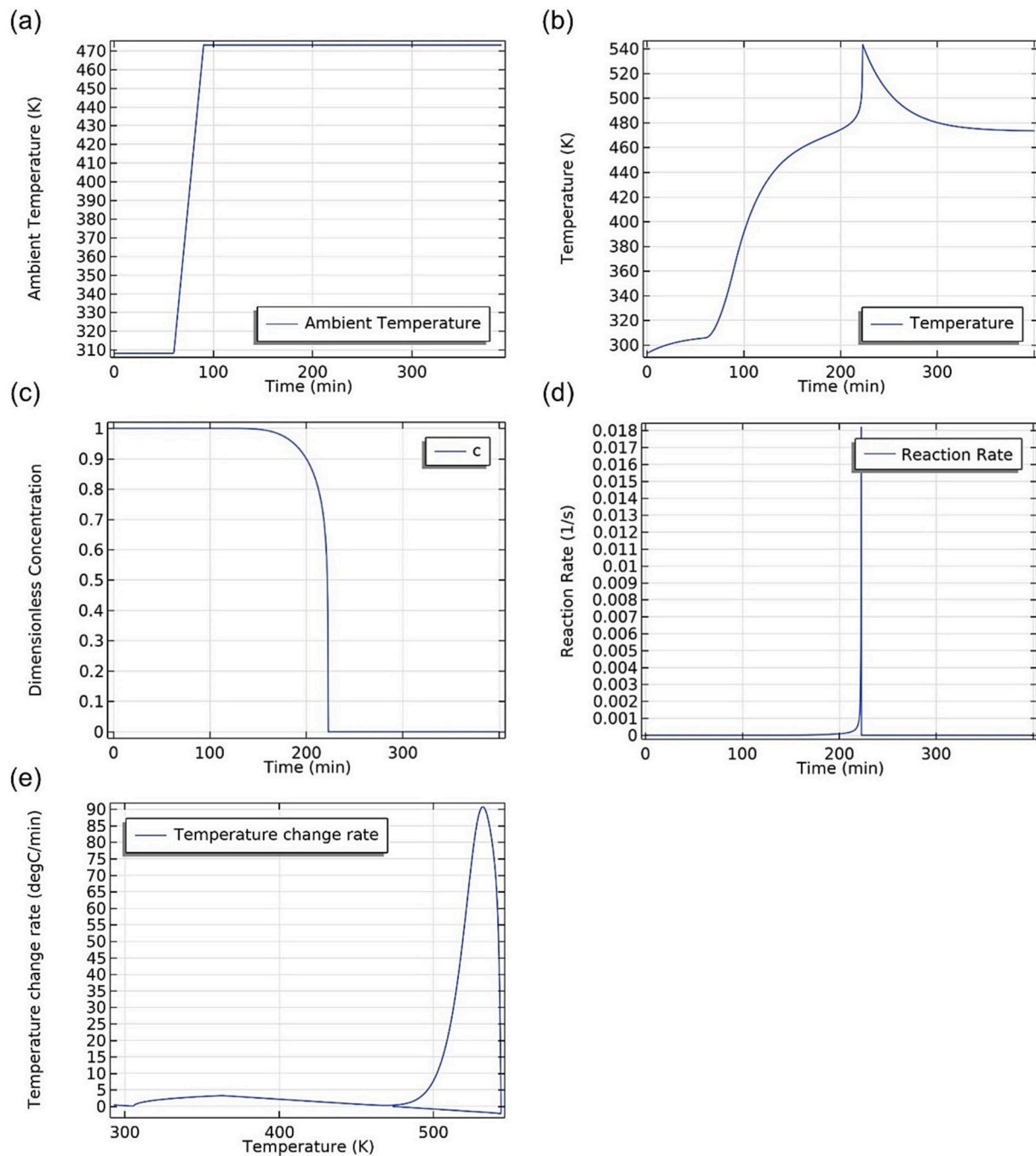**Fig. 3.** (a) Three-dimensional cylindrical cell and (b) computational mesh for its 2D cross-section.

Fig. 4. Illustration of (a) ambient temperature T_{amb}, (b) mean temperature, (c) mean dimensionless concentration of lithium in electrolyte, (d) reaction rate over time, and (e) temperature change rate.

4.2. TR estimation by MPINN

This subsection presents the results of TR estimation using the proposed MPINN. To validate the accuracy of the method in the estimation of temperature T and dimensionless concentration c, the estimated results were compared with numerical results shown in Section 4.1. The results of an ANN model of the same network structure as the MPINN were also compared to highlight the accuracy and robustness of the MPINN over the purely data-driven method. As summarized in Table 2, the MAEs of the estimated temperature and dimensionless concentration obtained by the MPINN and ANN with respect to reference data (when size of training data is 30,600) are 0.46 and 2.06e-4 and 1.17 and 2.28e-3, respectively, indicating that the MAEs of the proposed method are less

than those of the ANN by 0.71 and 2.07e-3; moreover, the RMSEs of the proposed method is less than that of the ANN by 1.57 and 4.01e-4, respectively. In general, the MPINN outperforms the ANN at every different sizes of the training data used for data-fitting. It can be observed that the accuracy improves as the size of the training data increases, implying that training larger datasets normally brings more benefits. However, this is only possible at the cost of exponentially growing training time, and the training time increases much faster in case of the MPINN. Although, it takes much longer to optimize, it generally guarantees higher accuracy on unseen data points. The MPINN accurately estimated the evolutions of temperature and dimensionless concentration distributions over time, even at points with no labeled data (Fig. 6). Specifically, the ANN exhibited large errors in the interval
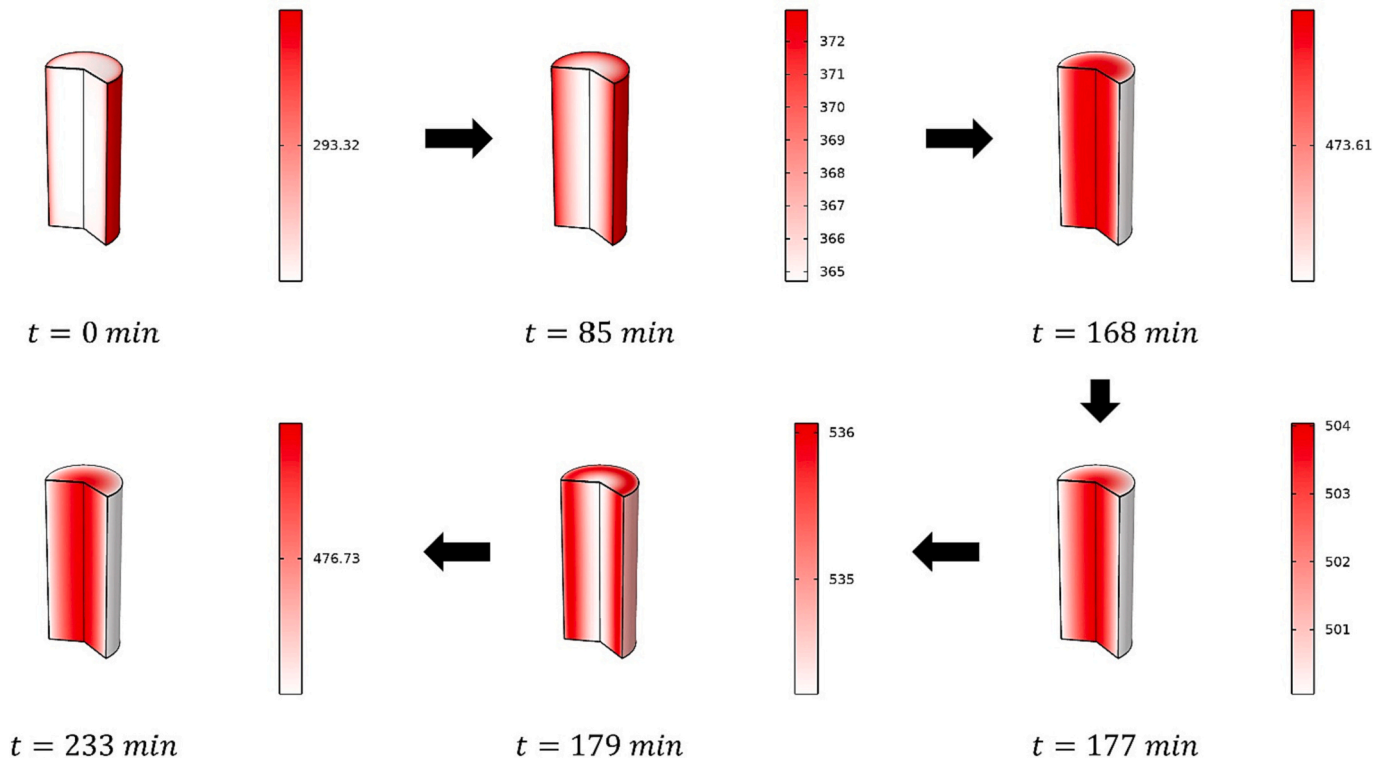
Fig. 5. Spatial TR simulation of a cylindrical LIB.

Table 2
Estimation results by MPINN and ANN. Best scores are marked in bold font.

		MPINN		ANN	
	Size of training data	MAE	RMSE	MAE	RMSE
Temperature	17,400	**3.02**	**8.71**	3.69	10.9
	24,000	**1.63**	**3.44**	2.81	6.50
	30,600 (reference)	**0.46**	**0.76**	1.17	2.33
	37,200	**0.45**	**0.76**	0.77	1.14
	43,800	**0.37**	**0.73**	0.65	0.96
Dimensionless concentration	17,400	**9.1e-4**	**1.9e-3**	9.9e-4	4.8e-3
	24,000	**5.1e-4**	**1.1e-3**	5.2e-4	2.9e-3
	30,600 (reference)	**2.1e-4**	**4.7e-4**	2.3e-4	7.7e-4
	37,200	**1.7e-4**	**4.2e-4**	1.9e-4	5.6e-4
	43,800	**1.0e-4**	**3.9e-4**	1.3e-4	4.4e-4
Training time (hours)	17,400	36		**1.1**	
	24,000	47		**1.2**	
	30,600 (reference)	52		**1.5**	
	37,200	59		**1.6**	
	43,800	70		**1.9**	

of t=162 min to t=199 min, as shown in Fig. 6(b), where the concentration started dropping and no label points were provided (the area inside the red dashed circle is magnified in the inset). This observation implies that an ordinary data-driven model cannot perform interpolation at points demonstrating a sudden change in pattern unless a label is provided to present clues about the change. Interestingly, the MPINN showed different behaviors because it was minimized on the ODE loss (Eq. (11)), which describes the evolution of dimensionless concentration over time, as well as other losses. This means that the MPINN presented

a significantly low level of overfitting. A similar observation can be made from Fig. 6(a) inside the specified circle. This phenomenon implies that the MPINN requires less instances of labeled data to accurately capture the underlying dynamics, i.e., extra information in the form of loss function fills the gap between two consecutive labeled points. This factor is a significant advantage for practical applications in which only the physical laws are known, but collecting or measuring the actual labeled data is challenging [11]. It should be noted that the number of labeled training data and network structures for the MPINN and ANN were set to be equal to ensure fair comparison.

In regard to the thermal runaway parameters estimated by the MPINN, the onset temperature occurred at $t = 183.6$ min and $T = 467.7$ K, the crucial temperature occurred at $t = 218$ min and $T = 488.1$ K, and the maximum temperature ($T = 543.5$ K) is reached at $t = 222.7$ min. Therefore, it takes 34.4 min and 39.1 min from the point of the onset temperature to reach the crucial temperature and the maximum temperature, respectively.

Fig. 7 presents further results regarding the estimated temperature at the cross-section of the cylindrical cell (Fig. 7(a)). From a cross-sectional viewpoint, the temperature distribution is symmetric with respect to the center point because the external heat that interacts with the cell is uniform throughout the boundaries. Because the heat inside the cell propagates significantly faster ($k_y \gg k_x$) along the y-axis (or axial direction) than the x-axis (or radial direction), the temperature gradient is sufficiently large and is thus visible only horizontally. Fig. 7(b) and (c) show the estimated temperature distributions at t=133 min by the MPINN and ANN, respectively, which emphasize this gradient symmetry along the x-axis. Unlike the MPINN output, which exhibits a perfect bell-shaped curve, the ANN output is relatively less symmetric. This implies that the ANN fails to accurately capture symmetricity, disobeying one of the physical laws. More specifically, the estimation results are compared in relation to the relative percent error (RPE) in Fig. 7(d) and (e) at t=133 min and t=210 min, respectively. In general, MPINN demonstrates better symmetricity and lower RPE than ANN. Observing the RPE distributions of the MPINN and ANN, the MPINN exhibits a relatively
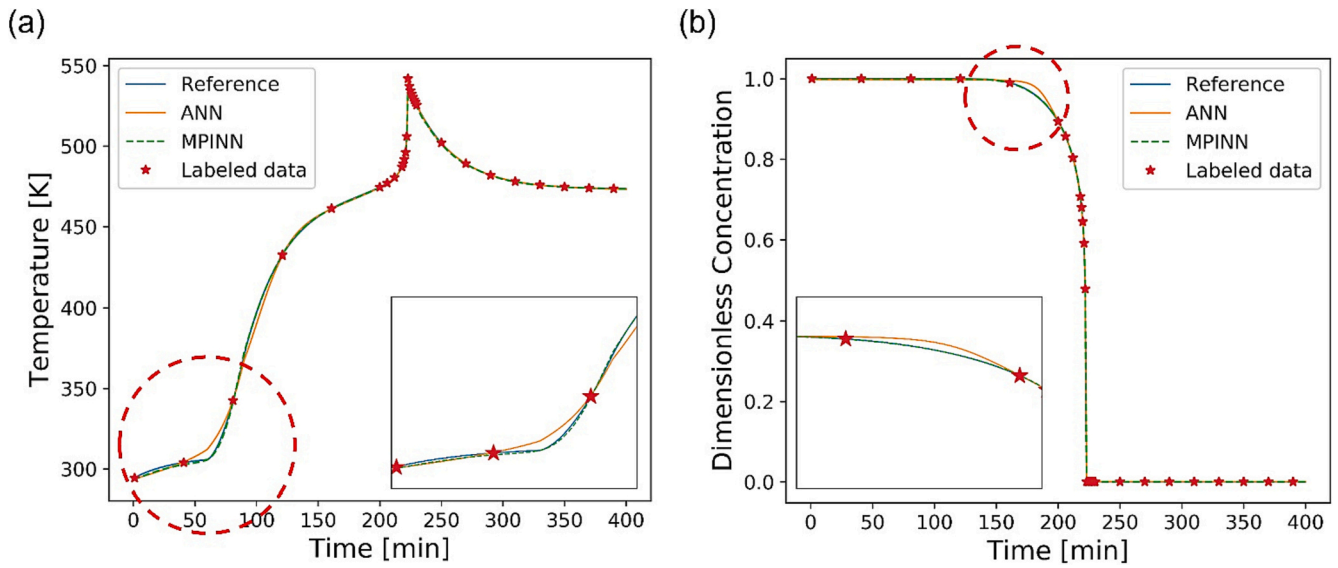
Fig. 6. TR estimation results of the MPINN and ANN w.r.t. reference data; (a) temperature and (b) dimensionless concentration.
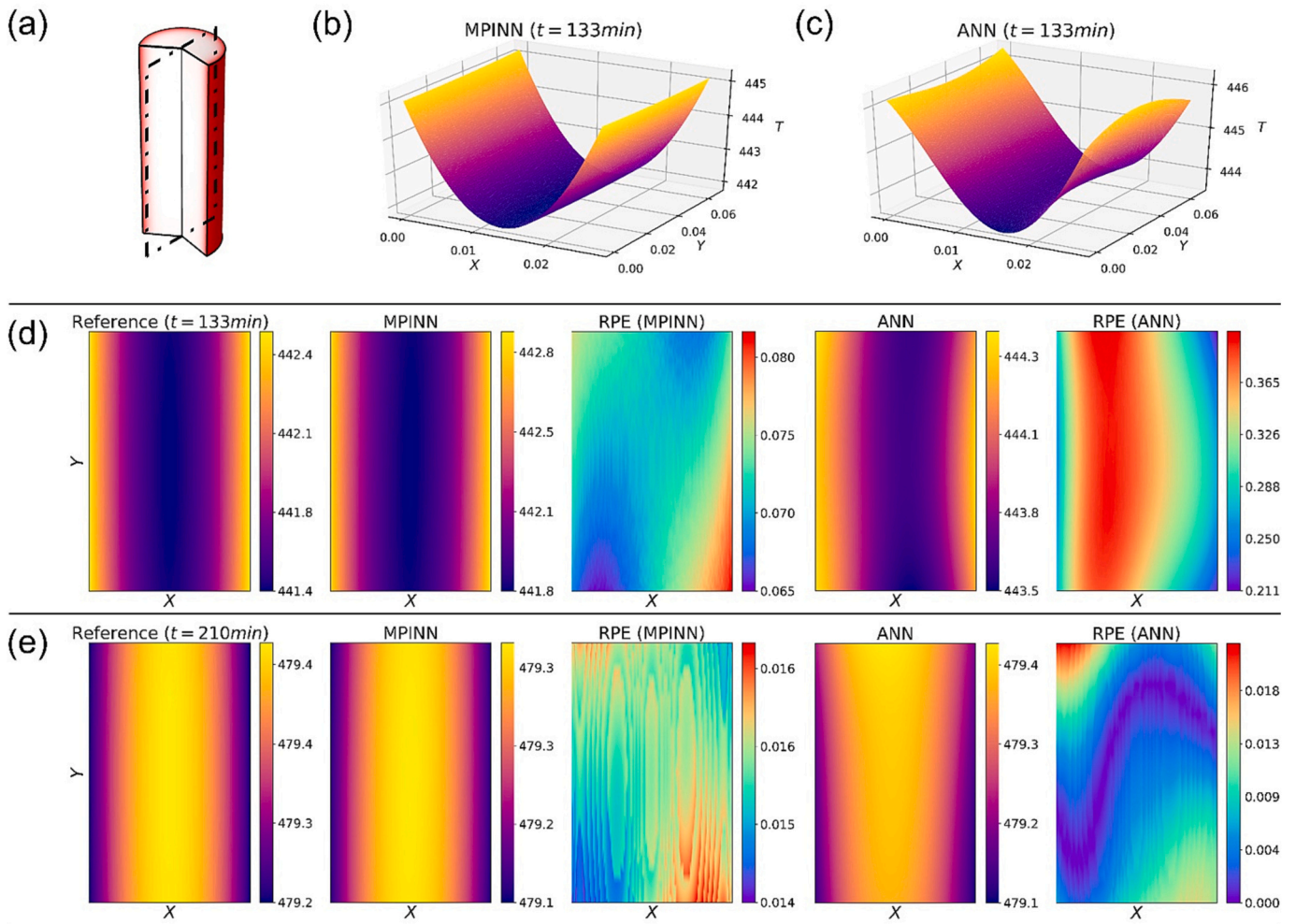

Fig. 7. (a) Cross-section of cylindrical cell. (b) Estimated temperature at t=133 min by the MPINN. (c) Estimated temperature at t=133 min by the ANN. (d) Comparative estimation results at t=133 min. (e) Comparative estimation results at t= 210 min.

higher error near the boundaries, whereas the ANN exhibits a more evenly distributed error across the domain. This trend can be attributed to the minimization of the MPINN on the boundary condition loss function separately from other loss functions. Even though the boundary condition loss is considered during optimization, sufficient minimization of this loss function cannot be guaranteed to satisfy the boundary condition and no errors at each point on the boundaries. All loss functions comprising the total loss of Eq. (8) should be equally minimized; however, the different levels of non-convexity inherent to each loss hinder uniform minimization. The next subsection discusses how the learning-rate annealing technique addresses this issue during training.

4.2.1. Effect of learning rate annealing

The learning rate annealing (LRA) algorithm discussed in Section 2.2 was leveraged to balance the interaction between multiple loss terms. To validate the effect of the algorithm in training the MPINN, the estimated outputs and training loss were analyzed for a case with and without the LRA. Fig. 8 depicts the estimated temperature (Fig. 8(a)), estimated dimensionless concentration (Fig. 8(b)), and loss over training iteration (Fig. 8(c)). The model optimized with the LRA exhibited significantly better estimation performance, particularly around the TR marked by red dashed circle in the figure. In contrast, the performance of the model optimized without the LRA was considerably worse than its counterpart when they were trained for the same number of iterations (210,000). In general, this model exhibited a smoother loss curve throughout the process; however, its convergence rate was slower than its counterpart. Moreover, it exhibited a higher loss value while reaching almost a flat curve; hence, there is no guarantee of further drastic loss reduction. In contrast, the model optimized with the LRA demonstrated high instability with large fluctuations in the early phase, but it stabilized after approximately 80,000 iterations and eventually resulted in a
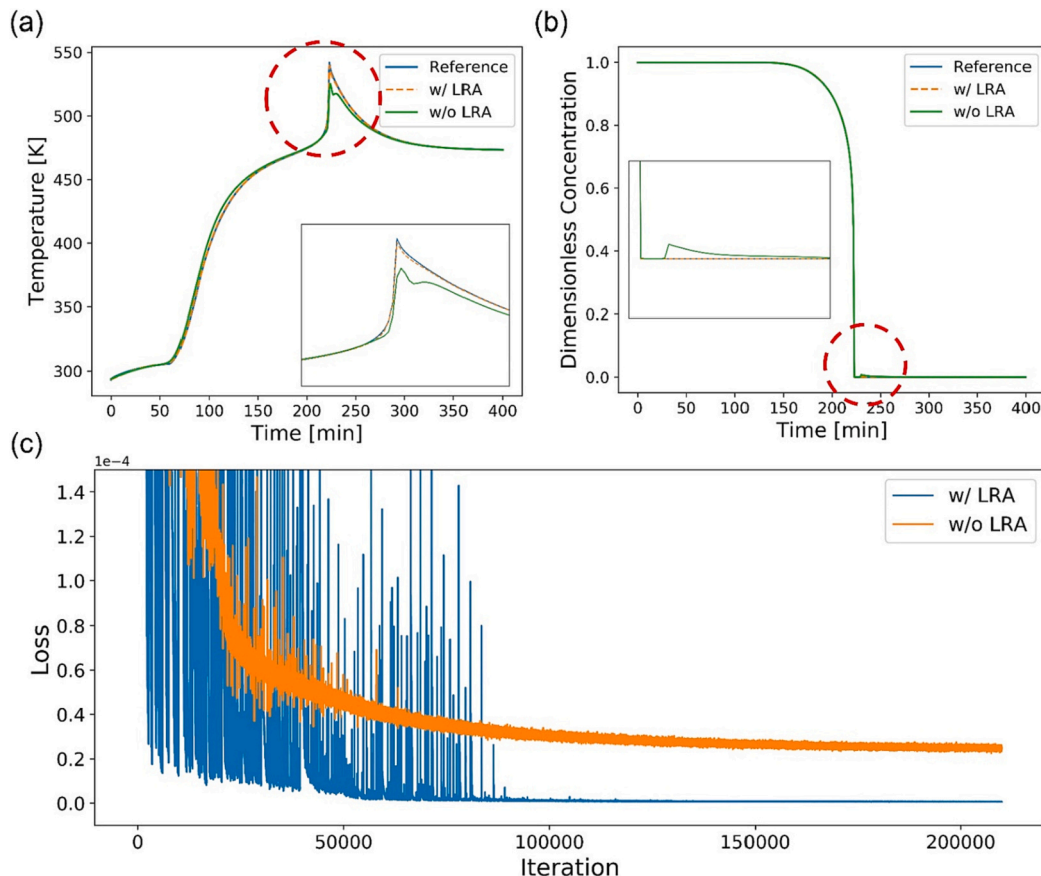
Table 3
Estimation results by MPINN with and without LRA. Best scores are marked in bold font.

		MPINN w/ LRA	MPINN w/o LRA
Temperature	MAE	**0.46**	1.67
	RMSE	**0.76**	2.79
Dimensionless concentration	MAE	**2.06e-4**	3.18e-3
	RMSE	**4.66e-4**	8.10e-4
Loss	MSE	**6.22e-7**	2.46e-5

significantly lower loss value of two orders of magnitude (Table 3). Considering that the estimated output of the model without the LRA demonstrated a large error near the TR point, the presence of the LRA is critical for the stable and sufficient convergence of the MPINN. Table 3 summarizes the quantitative results of the estimated outputs and training loss.

4.2.2. Drawbacks related to MPINN and its potential

Although the MPINN yielded promising results and higher estimation performance than the ANN, the major drawback of the proposed MPINN is that it has limited usability under particular circumstances in comparison to the conventional FEM. Technically, while both the MPINN and ANN use labeled data for training, the FEM does not need them for modeling. The availability of data labeling becomes a problem in situations where measurement or observation is costly or even impossible. A great example of the absence of measurement is prognosis because future measurements cannot be obtained in advance unless predicted. Therefore, MPINNs may still not be a preferred choice over FEM in a practical sense. However, in many cases, PINNs can be trained without labeled data [10,13,16]. To support this claim, the proposed MPINN was trained in a semi-supervised and unsupervised manner; the

Fig. 8. (a) Estimated temperature, (b) dimensionless concentration estimated by the MPINN, and (c) training loss when training the MPINN.

Table 4
Pros and cons of the FEM, MPINN, and ANN for limited amount of labeled data. Best choices are marked in bold font.

	FEM	MPINN	ANN
Accuracy	**Extremely high**	High	Medium
Training time	Long	Long	**Short**
Inference time	**Instantaneous**	**Instantaneous**	**Instantaneous**
Label necessity	**No**	Limited	Yes
Surrogate modeling	No	**Limited**	No

following sections discuss its operation under specific circumstances. More importantly, MPINN is capable of surrogate modeling in limited circumstances, as discussed in Section 4.3.2. The FEM is widely known to fail in generalizing unseen data. Table 4 summarizes the advantages and disadvantages of these methods in the presence of a limited amount of labeled data [10]. Although the FEM yielded the highest accuracy without the requirement for labeled data, its training time was relatively high and surrogate modeling cannot be implemented. The major drawbacks of the FEM can ultimately be complemented by the advantages of MPINN. The following subsection discusses the potential of the proposed MPINN as an alternative to conventional FEM.

4.3. Practical applications

This subsection presents case studies related to semi-supervised learning, unsupervised learning, and surrogate modeling using the proposed MPINN in more practical scenarios. Semi-supervised learning refers to a scenario in which a small subset of the entire data is exploited to train a model and then predict the remaining unseen but time- or domain-wise correlated parts [35]. In the field of prognostics and health management, the future system state must be predicted in a semi-supervised manner, given past states. Unsupervised learning is a type of model training that does not use labeled data. Surrogate modeling refers to obtaining the model solution for different values of problem parameters, such as boundary conditions and material properties. This is crucial in the design optimization stage because a large number of test conditions must be evaluated to finalize the product design. This can significantly reduce the cost and repetitive tasks. Therefore, the aforementioned case studies reflect the possible practical applications of the proposed model.

4.3.1. Case study: Semi-supervised and unsupervised learning for TR prediction

In semi-supervised learning settings, two modifications were made to investigate the feasibility of the MPINN. First, the prediction results of the positive electrode decomposition model were analyzed in lieu of the previously used electrolyte decomposition model because the former demonstrates significantly higher accuracy than the latter. Thus, the proposed MPINN was investigated in terms of the effect of data-fit loss and different chemical reaction degradations. Second, the data-fit loss (Eq. (6)) was used in the first half of the training phase, but it was omitted in the second half. The boundary between the first and second halves was determined heuristically, but one should consider which part of the TR has already been observed and which part must be predicted for prognostic purposes.

Fig. 9 shows the prediction results under various circumstances, i.e., three different T_{amb}s, which are indicated by blue dashed lines in Fig. 9 (a), (b), and (c). Specifically, T_{amb} starts off at 308.15 K and remains constant for a while until it increases linearly (Fig. 9(a) and (b)) or as a step function (Fig. 9(c)) until it reaches 473.15 K in all three scenarios. Note that T_{amb} is the control variable that determines the overall TR characteristics; it also reflects the time-dependent heat propagation profile in experimental settings, as mentioned in Section 3.1. In addition, T_{amb} represents the ambient temperature controlled by a cooling system in a battery thermal management system, suggesting that the analysis

would be helpful in designing a battery thermal management system. Hence, one may be interested in the predicted performance of the proposed model when T_{amb} is varied for design optimization in diverse usage profiles during product development.

The observed part, i.e., the first half with data-fit loss, is shaded in green, whereas the area of interest for prognostic measures (i.e., the second half without data-fit loss) is shaded in blue in Fig. 9. Note that the linearly increasing part of T_{amb} is placed inside green and blue regions in Fig. 9(a) and (b), respectively, to demonstrate that the MPINN can forecast the TR regardless of the characteristics of the observed data in the first half. Fig. 9(c) shows a good fit of an MPINN prediction to the reference data for a highly factitious and randomized T_{amb} represented in the form of multistep functions. To further demonstrate the effectiveness of the MPINN, it was compared with ANN; the results of the MPINN for the temperature (Fig. 9(a), (b), and (c)) and dimensionless concentration (Fig. 9(d), (e), and (f)) were found to be similar to those of the ANN in the green region, but they differed by a large margin in the blue region, where prediction was performed. This result is reasonable because ANNs and most other DNNs are known to fail in extrapolating unless prior knowledge is given for generalization to out-of-distribution [36]. In contrast, the MPINN demonstrated good extrapolation performance because the unseen part was informed during optimization in the form of loss functions or inductive bias [37]. It also implies that the MPINN has not been overfitted to the training data. Table 5 presents a quantitative evaluation of the results.

Following the evaluation of semi-supervised learning, unsupervised learning was investigated. Although it has been reported that several PINNs do not require labeled data, this is not true for all previously studied PINNs [12,38–40]. This is because the convergence of PINNs significantly relies on the type and nonlinearity of loss functions involved; those that require the assistance of labeled data for better convergence must be trained differently, and this is currently an open research topic. Similarly, TR generally requires labeled data for PINN convergence, as discussed in Section 4.2 and the case of semi-supervised learning.

Moreover, Fig. 10 demonstrates that labeled data may not be mandatory under a particular condition; this figure presents the prediction outcomes of the positive electrode decomposition model (Fig. 10 (a)) and electrolyte decomposition model (Fig. 10(b)). It can be observed that the MAE and RMSE in both results are higher than those of the first model, $T_{amb,\ 1}$, of the semi-supervised setting, implying that labeled data are necessary for better fitting to the reference. However, unlike the electrolyte decomposition model, which presents large errors around the TR point, the positive electrode decomposition model ensured tolerable accuracy even without supervision. This difference can be attributed to the complexity of landscape loss for different PDEs, as discussed by Krishnapriyan et al. [14]. Even for the same governing laws, the loss landscape can be smooth or extremely complex depending on the values of coefficients in PDEs.

To illustrate the effect of different PDEs in optimization, the temporal (T_t) and spatial (T_{xx} and T_{yy}) temperature gradients of both models for comparative analysis are plotted, as shown in Fig. 11. The plots in Fig. 11(a) show an increase in the gradient magnitude at approximately t=60 min, followed by a decrease starting at t=100 min, implying that relatively high gradients must be computed during this period. This observation explains the slight error found in the temperature prediction results of the MPINN from t=60 min to t=100 min in Fig. 10(a). However, the error was generally low because the change in gradient magnitude was not significant. In contrast, a significant change was observed in the gradient at t=224 min in the electrolyte decomposition model (Fig. 11(b)). Owing to the sudden jump in the gradient, the complexity of the loss landscape significantly increased, leading to insufficient convergence at a particular point and relatively large prediction error at the TR point, as observed in Fig. 10(b). In summary, the use of labeled data for supervision is not always mandatory for predicting the positive electrode decomposition model, but it is for the
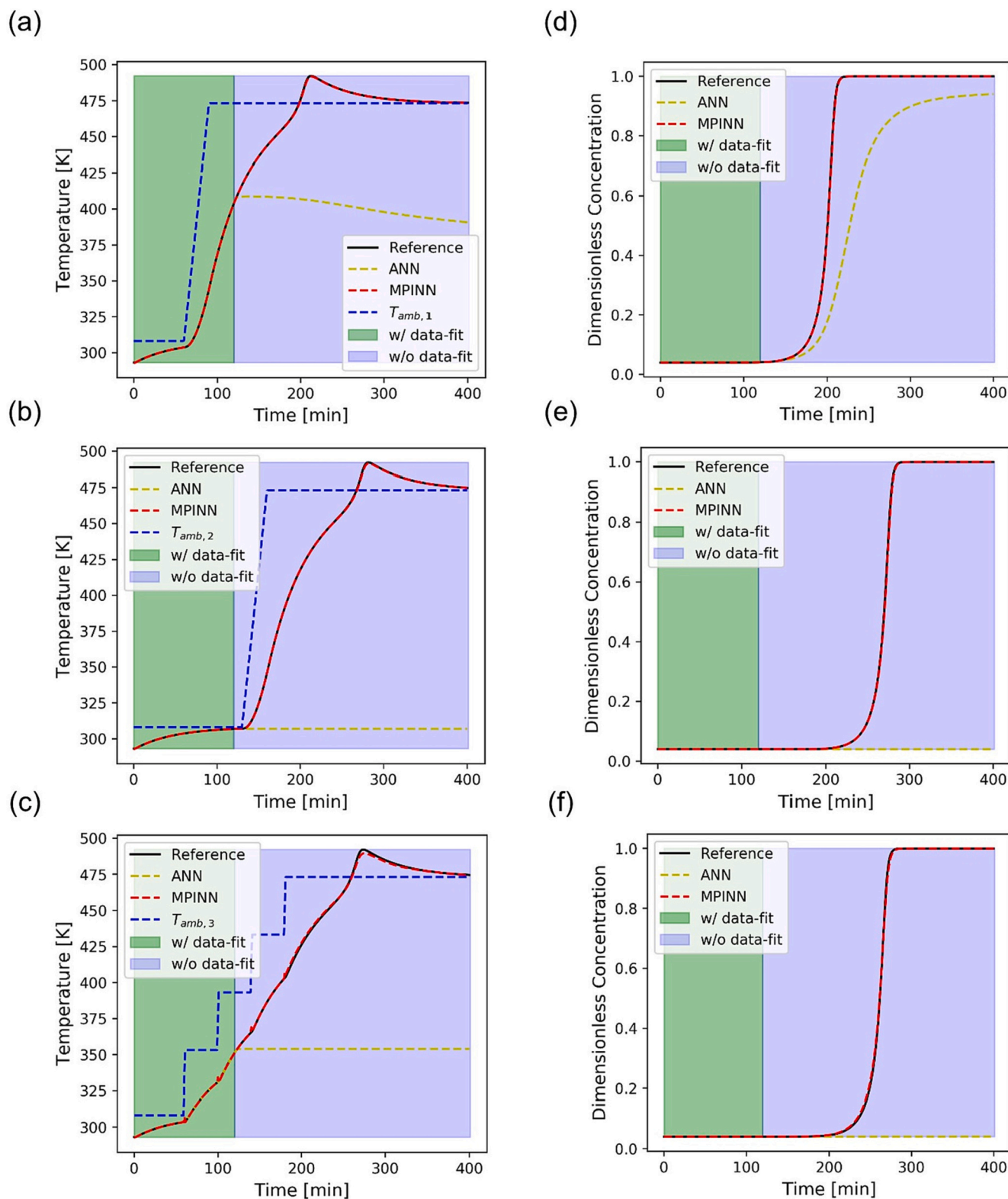
Fig. 9. Semi-supervised settings: Predicted temperature and dimensionless concentration over time for $T_{amb,\,1}$, $T_{amb,\,2}$, and $T_{amb,\,3}$ are shown in (a), (b), and (c), and (d), (e), and (f), respectively.

electrolyte decomposition model owing to the nontrivial PDE of the model.

4.3.2. Case study: surrogate modeling

This subsection discusses the potential application of the MPINN as a surrogate model for TR estimation. Assuming that one is interested in

estimating the response variables, T and c, as a function of T_{amb} with a predefined space and time, its mathematical formulation can be given by: $T, c = MPINN(x, y, t, T_{amb})$. In addition to the T_{amb} profile detailed in Fig. 4(a), two similar profiles (refer to Fig. S1 in Supplementary Material) and their associated datasets were added to the entire training dataset. In contrast to conventional FEM/FDM-based methods that

Table 5
Quantitative summary of predicted results under semi-supervised and unsupervised settings. "PE" and "E" inside brackets denote the positive electrode decomposition model and electrolyte decomposition model, respectively. Best scores are marked in bold font.

|			Semi-supervised learning		Unsupervised learning	
			MPINN	ANN	MPINN (PE)	MPINN (E)
$T_{amb,1}$	Temperature	MAE	**0.08**	47.46	**1.29**	12.30
		RMSE	**0.17**	59.96	**2.51**	21.57
	Dimensionless concentration	MAE	**5.70e-4**	0.10	**2.35e-3**	0.29
		RMSE	**2.34e-3**	0.19	**8.25e-3**	0.49
$T_{amb,2}$	Temperature	MAE	**0.12**	90.68	**5.47**	47.95
		RMSE	**0.25**	118.89	**9.62**	78.83
	Dimensionless concentration	MAE	**8.5e-4**	0.32	**0.03**	0.19
		RMSE	**3.46e-3**	0.54	**0.09**	0.40
$T_{amb,3}$	Temperature	MAE	**0.54**	49.05	**5.81**	57.59
		RMSE	**0.91**	67.11	**8.28**	85.58
	Dimensionless concentration	MAE	**1.5e-3**	0.34	**0.03**	0.20
		RMSE	**4.05e-3**	0.56	**0.10**	0.41

enable one model construction for a single T_{amb} profile, the MPINN can handle multiple T_{amb} profiles simultaneously.

This would be computationally beneficial when evaluating numerous operational profiles to ensure safety and reliability in LIB cells, modules, and packs using the Monte Carlo method for uncertainty quantification in the product development phase. After a model is optimized, it can be evaluated on the trained T_{amb} profiles, which takes approximately 0.01 s per evaluation. This is approximately 42,000 times faster than the computation time of COMSOL Multiphysics, which requires approximately 7 min to compute each T_{amb} profile. Fig. 12 illustrates the estimated temperature and dimensionless concentration at different T_{amb} profiles for the positive electrode decomposition model (Fig. 12(a) and (b)) and electrolyte decomposition model (Fig. 12(c) and (d)). As summarized in Table 6, the estimation performance is comparable to previous cases discussed in Sections 4.2 and 4.3.1 in terms of the MAE and RMSE, even though multiple T_{amb} profiles were trained

simultaneously. The MAE remained small for all cases, below 1.0 and 0.001 for the temperature and dimensionless concentration, respectively. Even though the estimation performance degrades when evaluating multiple profiles simultaneously, the reduced computational cost is the major advantage, implying that the proposed MPINN methodology can be leveraged as a surrogate model in more complex and diverse scenarios.

5. Conclusion

An MPINN was proposed in this study to estimate and predict TR in an LIB; further, its applicability to semi-supervised learning, unsupervised learning, and surrogate modeling was investigated. The proposed methodology featured four main characteristics as the key contributions. First, this study presented the first MPINN-based TR estimation in an LIB; the results of this study can be used in future research related to MPINNs to estimate and predict more sophisticated incidents of TR in real time. Second, the difference between positive electrode decomposition and electrolyte decomposition was highlighted from the perspective of PINN convergence. This study supported the claim that PINNs generally encounter convergence issues owing to drastic changes in gradients stemming from an inflection point. Hence, estimating the electrolyte decomposition model through the MPINN is more challenging because its chemical reactions are more substantial, instantaneous, and momentous. Third, the effects of data-fit loss and learning rate annealing to address the convergence issues were analyzed and demonstrated via case studies, which revealed that labeled data and learning rate annealing improve the MPINN estimation performance. Fourth, the MPINN was compared against an ANN to prove its effectiveness over standard data-driven methods. The MAE and RMSE of the proposed MPINN were less than those of the ANN by 0.71 and 1.57, respectively, when labeled data were used for training. The MPINN outperformed the ANN in terms of the MAE and RMSE by approximately 90.56 and 118.64, respectively, in the semi-supervised setting for TR prediction. In future studies, including additional chemical reactions and dynamics for charge and discharge during TR estimation, and focusing on validating the MPINN for more diverse input profiles that reflect the randomness of LIB usage and harsh environmental conditions are considered. In addition, a one-to-one comparison of the estimation and prediction results of MPINN with those of TR experiments using real batteries needs to be done to enhance the reliability of the proposed
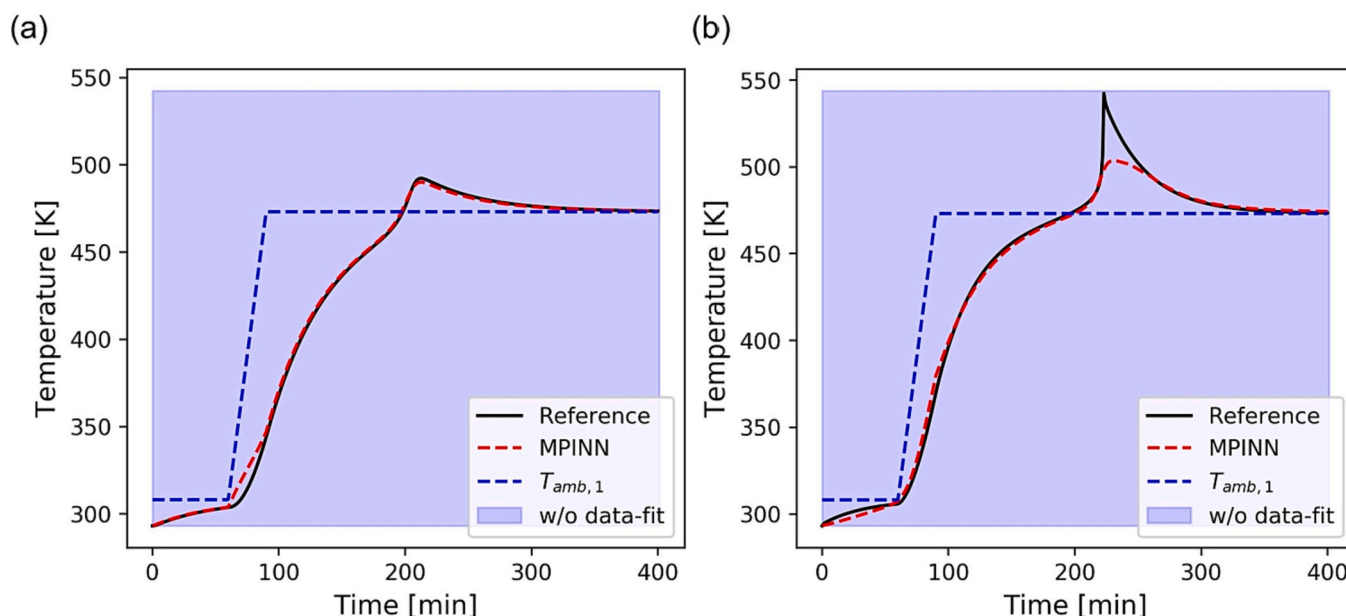
Fig. 10. Unsupervised settings: Predicted temperature over time for (a) positive electrode decomposition model and (b) electrolyte decomposition model.
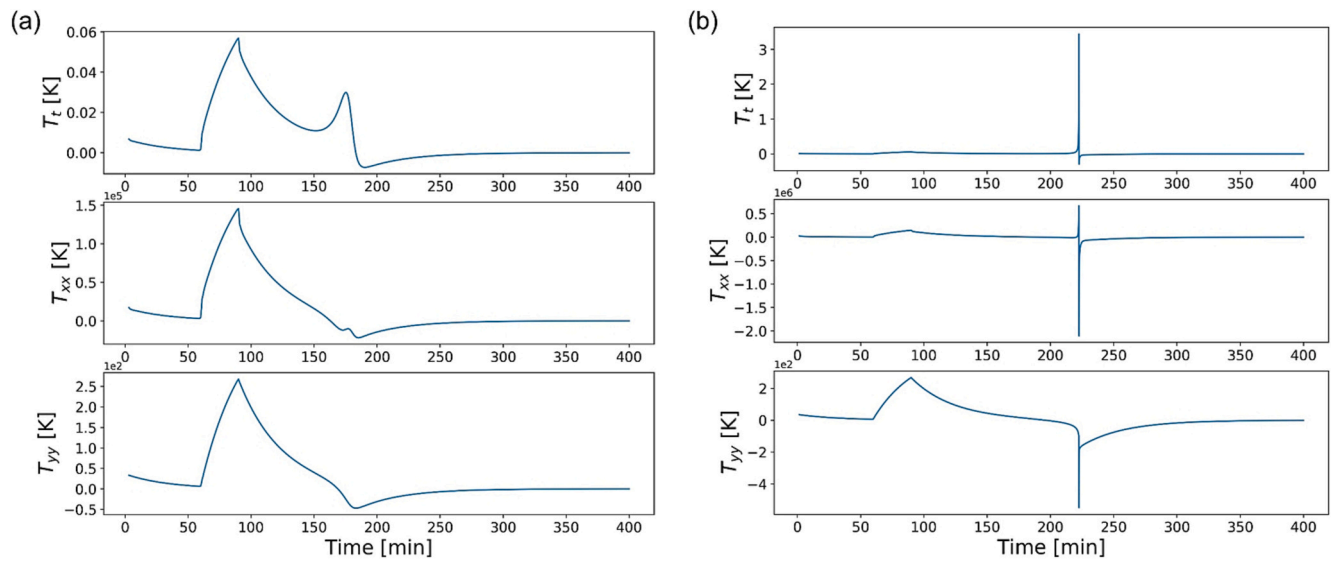
Fig. 11. Evolution of temporal (T_t) and spatial (T_{xx} and T_{yy}) temperature gradients for (a) positive electrode decomposition model and (b) electrolyte decomposition model.
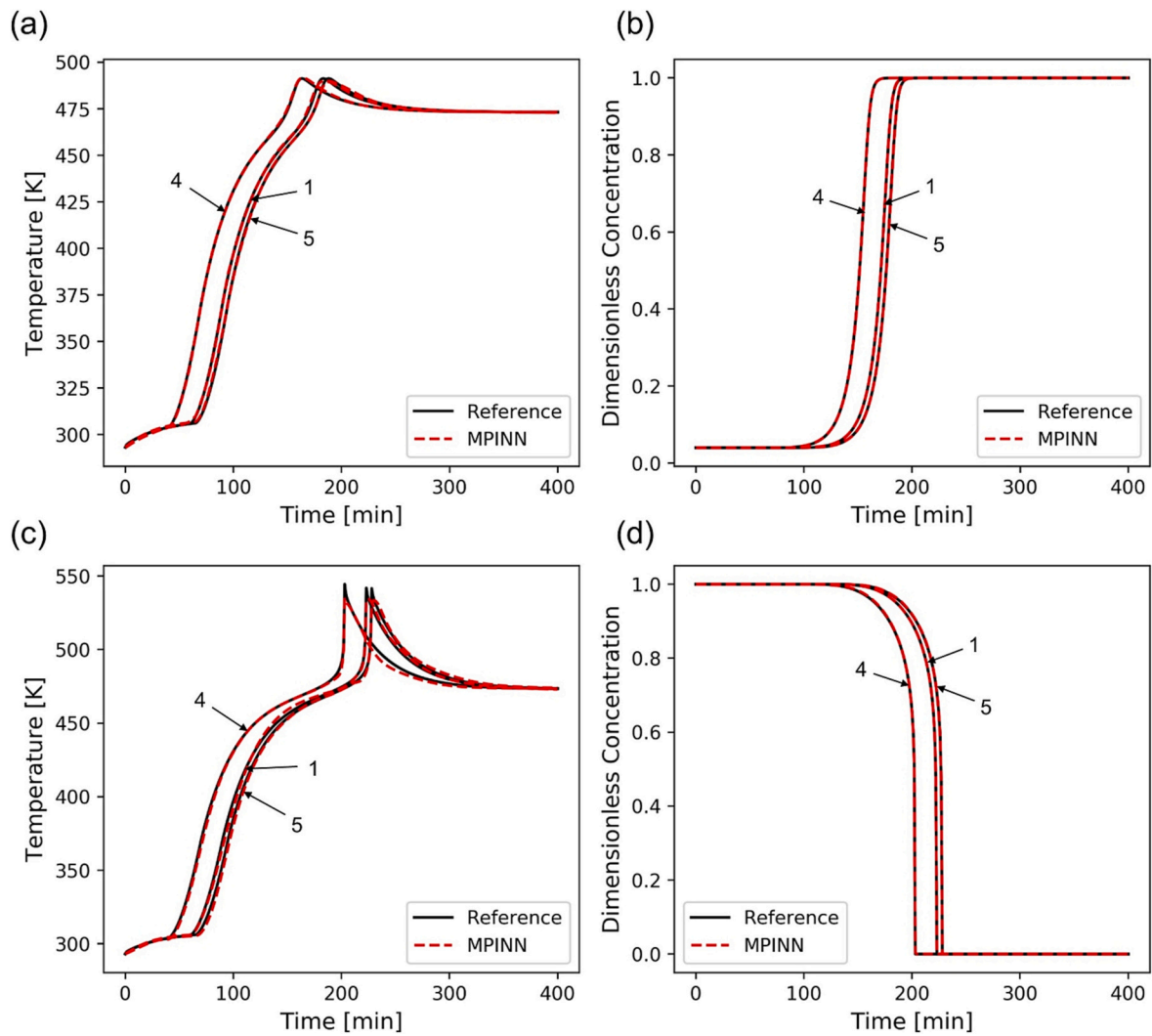

Fig. 12. Estimated temperature and dimensionless concentration at three different T_{amb} profiles for ((a) and (b)) positive electrode decomposition model and ((c) and (d)) electrolyte decomposition model. Numbers marked with arrows denote profile numbers.

Table 6

Quantitative summary of estimated results for positive electrode decomposition model and electrolyte decomposition model. T_{amb} profiles follow the plots specified in Fig. S1 of Supplementary Material.

			Positive electrode	Electrolyte
$T_{amb,\ 1}$	Temperature	MAE	0.51	0.97
		RMSE	1.44	2.44
	Dimensionless concentration	MAE	1.78e-4	8.14e-5
		RMSE	3.31e-4	2.25e-4
$T_{amb,\ 4}$	Temperature	MAE	0.30	0.99
		RMSE	1.01	2.24
	Dimensionless concentration	MAE	2.06e-4	1.52e-4
		RMSE	3.45e-4	4.48e-4
$T_{amb,\ 5}$	Temperature	MAE	0.60	0.90
		RMSE	1.54	2.36
	Dimensionless concentration	MAE	1.97e-4	1.41e-4
		RMSE	4.01e-4	4.71e-4

model.

Supplementary data to this article can be found online at https://doi.org/10.1016/j.est.2023.106654.

CRediT authorship contribution statement

Sung Wook Kim: Methodology, Conceptualization, Formal analysis, Writing- Original draft preparation, Writing- Reviewing and Editing. **Eunji Kwak:** Methodology. **Jun-Hyeong Kim:** Conceptualization. **Ki-Yong Oh:** Conceptualization, Formal analysis, Writing- Reviewing and Editing, Funding acquisition. **Seungchul Lee:** Writing- Reviewing and Editing, Funding acquisition, Supervision.

Funding

Declaration of competing interest

The authors declare that they have no known competing financial interests or personal relationships that could have appeared to influence the work reported in this paper.

Data availability

Data available on request from the authors.

References

[1] Q. Wang, P. Ping, X. Zhao, G. Chu, J. Sun, C. Chen, Thermal runaway caused fire and explosion of lithium ion battery, J. Power Sources 208 (2012) 210–224.

[2] P. Ping, Q. Wang, Y. Chung, J. Wen, Modelling electro-thermal response of lithium-ion batteries from normal to abuse conditions, Appl. Energy 205 (2017) 1327–1344.

[3] E. Kwak, J.H. Kim, S.H. Hong, K.Y. Oh, Detailed modeling investigation of thermal runaway pathways of a lithium iron phosphate battery, Int. J. Energy Res. 46 (2) (2022) 1146–1167.

[4] B. Mao, H. Chen, Z. Cui, T. Wu, Q. Wang, Failure mechanism of the lithium ion battery during nail penetration, Int. J. Heat Mass Transf. 122 (2018) 1103–1115.

[5] R. Zhao, J. Liu, J. Gu, A comprehensive study on li-ion battery nail penetrations and the possible solutions, Energy 123 (2017) 392–401.

[6] D. Ren, et al., An electrochemical-thermal coupled overcharge-to-thermal-runaway model for lithium ion battery, J. Power Sources 364 (2017) 328–340.

[7] A. Kriston, et al., External short circuit performance of graphite-LiNi1/3Co1/3Mn1/3O2 and graphite-LiNi0. 8Co0. 15Al0. 05O2 cells at different external resistances, J. Power Sources 361 (2017) 170–181.

[8] Z. An, K. Shah, L. Jia, Y. Ma, Modeling and analysis of thermal runaway in Li-ion cell, Appl. Therm. Eng. 160 (2019), 113960.

[9] P.J. Bugryniec, J.N. Davidson, S.F. Brown, Computational modelling of thermal runaway propagation potential in lithium iron phosphate battery packs, Energy Rep. 6 (2020) 189–197.

[10] L. Sun, H. Gao, S. Pan, J.-X. Wang, Surrogate modeling for fluid flows based on physics-constrained deep learning without simulation data, Comput. Methods Appl. Mech. Eng. 361 (2020), 112732.

[11] M. Raissi, A. Yazdani, G.E. Karniadakis, Hidden fluid mechanics: learning velocity and pressure fields from flow visualizations, Science 367 (6481) (2020) 1026–1030.

[12] S.A. Niaki, E. Haghighat, T. Campbell, A. Poursartip, R. Vaziri, Physics-informed neural network for modelling the thermochemical curing process of composite-tool systems during manufacture, Comput. Methods Appl. Mech. Eng. 384 (2021), 113959.

[13] S. Cai, Z. Wang, S. Wang, P. Perdikaris, G.E. Karniadakis, Physics-informed neural networks for heat transfer problems, J. Heat Transf. 143 (6) (2021).

[14] A. Krishnapriyan, A. Gholami, S. Zhe, R. Kirby, M.W. Mahoney, Characterizing possible failure modes in physics-informed neural networks, Adv. Neural Inf. Process. Syst. 34 (2021).

[15] S. Wang, Y. Teng, P. Perdikaris, Understanding and mitigating gradient flow pathologies in physics-informed neural networks, SIAM J. Sci. Comput. 43 (5) (2021) A3055–A3081.

[16] W. Ji, W. Qiu, Z. Shi, S. Pan, S. Deng, Stiff-pinn: physics-informed neural network for stiff chemical kinetics, J. Phys. Chem. A 125 (36) (2021) 8098–8106.

[17] Y. Shin, J. Darbon, G.E. Karniadakis, On the convergence of physics informed neural networks for linear second-order elliptic and parabolic type PDEs, arXiv preprint, 2020 arXiv:2004.01806.

[18] A.G. Baydin, B.A. Pearlmutter, A.A. Radul, J.M. Siskind, Automatic differentiation in machine learning: a survey, J. Mach. Learn. Res. 18 (2018) 1–43.

[19] R. Zhang, Y. Liu, H. Sun, Physics-informed multi-LSTM networks for metamodeling of nonlinear structures, Comput. Methods Appl. Mech. Eng. 369 (2020), 113226.

[20] E. Kharazmi, Z. Zhang, G.E. Karniadakis, Variational physics-informed neural networks for solving partial differential equations, arXiv preprint, 2019 arXiv:1912.00873.

[21] E. Kharazmi, Z. Zhang, G.E. Karniadakis, Hp-VPINNs: variational physics-informed neural networks with domain decomposition, Comput. Methods Appl. Mech. Eng. 374 (2021), 113547.

[22] R. Xu, D. Zhang, M. Rong, N. Wang, Weak form theory-guided neural network (TgNN-wf) for deep learning of subsurface single-and two-phase flow, J. Comput. Phys. 436 (2021), 110318.

[23] A.D. Jagtap, G.E. Karniadakis, Extended physics-informed neural networks (xpinns): a generalized space-time domain decomposition based deep learning framework for nonlinear partial differential equations, Commun. Comput. Phys. 28 (5) (2020) 2002–2041.

[24] J. Kim, K. Lee, D. Lee, S.Y. Jin, N. Park, DPM: A novel training method for physics-informed neural networks in extrapolation, arXiv preprint, 2020 arXiv:2012.02681.

[25] C.G. Fraces, H. Tchelepi, Physics informed deep learning for flow and transport in porous media, in: SPE Reservoir Simulation Conference, 2021.

[26] D. Lu, I.C. Christov, Physics-informed neural networks for understanding shear migration of particles in viscous flow, arXiv preprint, 2021 arXiv:2111.04684.

[27] E. Haghighat, D. Amini, R. Juanes, Physics-informed neural network simulation of multiphase poroelasticity using stress-split sequential training, arXiv preprint, 2021 arXiv:2110.03049.

[28] W. Mei, L. Zhang, J. Sun, Q. Wang, Experimental and numerical methods to investigate the overcharge caused lithium plating for lithium ion battery, Energy Storage Mater. 32 (2020) 91–104.

[29] G.-H. Kim, A. Pesaran, R. Spotnitz, A three-dimensional thermal abuse model for lithium-ion cells, J. Power Sources 170 (2) (2007) 476–489.

[30] T. Hatchard, D. MacNeil, A. Basu, J. Dahn, Thermal model of cylindrical and prismatic lithium-ion cells, J. Electrochem. Soc. 148 (7) (2001) A755.

[31] I. Esho, K. Shah, A. Jain, Measurements and modeling to determine the critical temperature for preventing thermal runaway in Li-ion cells, Appl. Therm. Eng. 145 (2018) 287–294.

[32] L. Yiding, W. Wenwei, L. Cheng, Y. Xiaoguang, Z. Fenghao, Multi-physics safety model based on structure damage for lithium-ion battery under mechanical abuse, J. Clean. Prod. 277 (2020) 124094.

[33] A.M. Bizeray, S. Zhao, S.R. Duncan, D.A. Howey, Lithium-ion battery thermal-electrochemical model-based state estimation using orthogonal collocation and a modified extended Kalman filter, J. Power Sources 296 (2015) 400–412.

[34] J. Allen, Review of polymers in the prevention of thermal runaway in lithium-ion batteries, Energy Rep. 6 (2020) 217–224.

[35] J.E. Van Engelen, H.H. Hoos, A survey on semi-supervised learning, Mach. Learn. 109 (2) (2020) 373–440.

[36] D. Berend, et al., Cats are not fish: deep learning testing calls for out-of-distribution awareness, in: Proceedings of the 35th IEEE/ACM International Conference on Automated Software Engineering, 2020, pp. 1041–1052.

[37] P.W. Battaglia, et al., Relational inductive biases, deep learning, and graph networks, arXiv preprint, 2018 arXiv:1806.01261.

[38] M. Raissi, P. Perdikaris, G.E. Karniadakis, Physics-informed neural networks: a deep learning framework for solving forward and inverse problems involving nonlinear partial differential equations, J. Comput. Phys. 378 (2019) 686–707.

[39] K. Shukla, P.C. Di Leoni, J. Blackshire, D. Sparkman, G.E. Karniadakis, Physics-informed neural network for ultrasound nondestructive quantification of surface breaking cracks, J. Nondestruct. Eval. 39 (3) (2020) 1–20.

[40] F. Sahli Costabal, Y. Yang, P. Perdikaris, D.E. Hurtado, E. Kuhl, Physics-informed neural networks for cardiac activation mapping, Front. Phys. 8 (2020) 42.